

Reactive ion plasma etched surface relief gratings for low/medium/high resolution spectroscopy in astronomy

Hanshin Lee^{a,*} and Menelaos K. Poutous^b

^aUniversity of Texas at Austin, McDonald Observatory, Austin, Texas, United States

^bUniversity of North Carolina at Charlotte, Department of Physics and Optical Science, Charlotte, North Carolina, United States

Abstract. We report the fabrication of a binary-phase proof-of-concept astronomical diffraction grating embedded in a quartz substrate via reactive ion plasma etching. This grating operates at the first diffraction order within the 450 to 750 nm wavelength band. It features 1400-nm-deep, 188-nm-wide binary grooves at a 566-nm pitch, or 1767 lines/mm groove density, over a 25.4×25.4 mm² area. A high depth-to-width ratio ($\sim 8:1$ in this case) is one of the keys to near-theoretical diffraction efficiency being attained by the fabricated grating (94% at center wavelength and 70% at band edges) over a broad bandpass (>200 nm). This performance is also attributed to high-resolution micro-lithographic electron-beam patterning and anisotropic reactive ion etching process fabrication techniques. These types of binary gratings can potentially be high-throughput alternatives to Volume-Phase Holographic Gratings (VPHGs) for general spectroscopic applications. When scaled to appropriate sizes for astronomy, such gratings can serve as main or cross dispersion elements in low-, medium-, and high-resolution spectrographs not only in ground-based telescopes but also in those subject to challenging environmental conditions such as in space observatories. © The Authors. Published by SPIE under a Creative Commons Attribution 4.0 International License. Distribution or reproduction of this work in whole or in part requires full attribution of the original publication, including its DOI. [DOI: [10.1117/1.JATIS.8.4.045002](https://doi.org/10.1117/1.JATIS.8.4.045002)]

Keywords: surface relief gratings; reactive ion etching; micro-lithography; astronomical spectroscopy.

Paper 22071G received Jul. 8, 2022; accepted for publication Oct. 5, 2022; published online Oct. 28, 2022; corrected Dec. 13, 2022.

1 Introduction

Attaining high efficiency in throughput is a fundamental and yet challenging task for any astronomical instrument builder. The growing need to observe fainter and fainter astronomical targets makes this task even harder, but steady progress is being made in multiple fronts, such as (1) building larger telescopes, (2) making delivered point spread functions smaller with high Strehl ratios, and (3) engineering more efficient reflective, transmissive, and diffractive optical components. Although there are efforts being made in (1) and (2), in the context of the Extremely Large Telescopes (ELTs)^{1,2} and their adaptive optics (AO) systems,³ with major improvement expectations, progress in (3) can also make significant gains in the overall efficiency of instruments. Together, a quantum leap in the overall throughput gain seems possible in the coming decade. As part of our contribution to the progress in the latter front, we developed a proof-of-concept (POC) surface relief diffraction grating using a reactive ion-plasma etch (RIPE) process to transfer a nano-scale grating structure permanently into a substrate surface. This resulted in an optomechanically robust diffractive device that is applicable, once appropriately scaled in area, to low/medium/high-resolution spectroscopy in astronomy.

This POC RIPE grating was designed to have a binary-phase linear profile on a quartz substrate, with a line pitch of 566 nm (or a line density of 1767 lines/mm), duty cycle of 33%, and etch depth of ~ 1400 nm. The operating bandpass of the grating spans from 450 to 750 nm, and the angle of incidence (AOI) from the substrate medium is 19.4 deg (blaze wavelength of 550 nm). Under these conditions, rigorous coupled wave analysis (RCWA) simulations

*Address all correspondence to Hanshin Lee, lee@astro.as.utexas.edu

of the grating predicted that, in both polarizations, the zeroth-order component was substantially suppressed whereas the first-order transmission was highly enhanced, with 95% to 98% peak performance. The analysis also predicted the unpolarized first-order transmission diffraction efficiency (DE) to be higher than 70% over a wide wavelength range (≥ 200 nm). Our spectral measurement of the fabricated grating confirmed these predictions and showed that the measured first-order transmission closely follows the theoretical transmission across the bandpass range. Some of the early results have been reported elsewhere.⁴ The present paper expands the narrative with much more detailed descriptions of the POC RIPPLE grating design optimization and fabrication process and results from in-process spectral tests to monitor etch depth (Sec. 2). New spectral measurements in the zeroth-, first-, and extra-orders are made to further quantify the grating's performance and final etch depth determination (Sec. 3).

2 POC RIPPLE Grating Design and Fabrication

2.1 Design

The spectral distribution of the diffracted light through this POC grating is described by the standard grating equation, where the AOI (α) and the line pitch (p) control the angle of diffraction (AOD) (β) of the diffracted orders (m) at a given wavelength (λ) [Fig. 1]. It is worth noting that n is the refractive index of the substrate at λ , α is defined in the substrate, and β is in air. For a fixed λ , the choice of α and p can also determine the number of non-evanescent propagation orders into which the efficiency of the diffraction order of interest can leak. Hence, for first-order gratings such as the POC RIPPLE grating designed here, these parameters are chosen to minimize the power in undesired diffraction orders. The line width (w) and the etch depth (d) are then primarily used to maximize the efficiency in the main diffraction order. A grating profile other than binary-phase may also influence overall efficiency. However, for near-wavelength grating periods with subwavelength features, as in the POC gratings (i.e., $\lambda/p \rightarrow 1$), our experience indicates that non-binary profiles have no clear advantage; instead fabrication complications are inevitable.

$$\frac{m\lambda}{p} = n \sin \alpha - \sin \beta. \quad (1)$$

The POC grating was designed to have a binary phase profile on a standard photolithographic mask quality quartz substrate. We chose $p = 566$ nm from one of the grating designs used for a fiber integral field unit spectrograph under construction.⁵ The operating bandpass spanned from 450 to 750 nm. α was nominally set to 19.4 deg. The grating depth (d) and groove width (w) were numerically optimized using RCWA simulations to maximize the first-order unpolarized DE in air.

In detail, this optimization process involved a three-dimensional cube of DE modeled with variable w , d , and λ , where w and d spanned ranges from $p/10$ to $p/1.1$, and from 0 to 3 μm , respectively [Fig. 2(a)]. The model cube shows slowly varying multiple efficiency peaks, mostly along the depth dimension. These peaks evolved in shape, overall efficiency, and location in the parameter space. Those located at deeper d tended to exhibit narrower width along the λ -axis compared with those at shallower d . The simulations also indicated that the efficiency between the two incident polarizations was best balanced near $w/p \sim 1/3$, and this balance tended to result in higher overall efficiency over wider wavelength ranges at depths around $d \sim 1400$ nm. As shown in Fig. 2(b), the efficiency terrain around the optimal depth and duty cycle varies slowly and smoothly. This allowed for fine-tuning the parameter selection for trade-offs between fabrication complexity and spectral bandpass efficiency as part of the astronomical spectrograph design process, without substantial impact on the overall performance. This, on the flip side, could be indicative of leniency in depth and line width control during the patterning and etching process.

Figure 2(c) shows a wavelength trace at $d = 1400$ nm, indicating a well-balanced efficiency between both incident polarizations. The curve peaks at 96.4% and remains higher than 70% over a wide (~ 230 nm) wavelength range with the full width at half maximum broader than

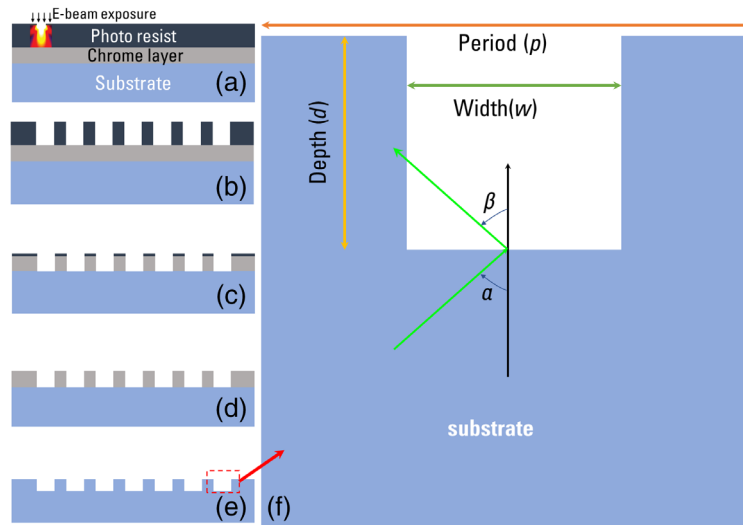


Fig. 1 An illustration of a binary-phase RIPLE grating and its fabrication process. (a) A grating line pattern is written in a thin layer of photo-resist by electron-beam exposure. (b) The developed photoresist is removed from the exposed spaces, uncovering the underlying chromium layer. (c) The chromium layer is etched-out from the photoresist grating grooves, leaving the substrate surface exposed. (d) The resist layer is washed away. (e) The grating grooves are etched into the substrate, using the chrome lines as a mask. (f) Schematic of a single grating period structured, with the feature parameters marked. The duty cycle is defined by w/p .

300 nm. One clear indication from this design process is that high overall efficiency calls for relatively deep-etched grooves between $d \sim 1300$ nm and 1500 nm, resulting in $d/w \sim 7.5$. We note that such aspect ratios are higher than the typical ranges (i.e., $d/w \sim 4$ or less) used in the micro-fabrication community and acknowledge that there are specialized processes (e.g., Bosch and cryogenic etching processes) that can achieve even higher aspect ratios.⁷ Though outside the scope of this report, we note that this trend appears true for RIPLE binary-phase grating designs operating at different α , λ , and p as to be reported elsewhere.

2.2 Fabrication

The POC grating fabrication followed the standard photo-mask patterning and etching process as previously illustrated (Fig. 1). A quartz substrate, with a 110-nm-thick metal chrome (Cr) layer on one surface and a thin electron-beam compatible photoresist coating over the Cr was used. The linear grating pattern was directly “written” on the photoresist, using an electron-beam exposure tool. The pattern was written over the central 25.4×25.4 mm² area in each of the four quadrants of a 152.4×152.4 mm² substrate (6.35-mm thick), which was then diced to four identical grating copies (called quadrants) to be used for process development trials [Fig. 3(a)]. Then, the Cr was wet-etched from the exposed areas to reveal the underlying quartz, and the remaining resist was stripped. The Cr-quartz grating profile is a hard mask for the plasma etch process. Smaller samples (called proxies) were cut in a 3×3 layout from one of the main grating quadrants for development of the etch process parameters [Fig. 3(b)]. A diamond/resin composite dicing blade was used to separate the proxies. For each dicing lane, multiple cutting strokes across the front and back side were needed to accommodate the mask thickness without excessive chipping. The samples were dry-etched using a reactive-ion plasma chamber (PlasmaTherm 7000), consisting of methyl-trifluoride (CHF_3) and oxygen (O_2) gases at a partial vacuum and under a 1000-W radio-frequency (RF) driving signal. The plasma radicals preferentially etch the exposed quartz, removing the material at a rate controlled mainly by the RF signal, the pressure in the chamber, and the replenishing flow rate of the reactive gases. After the completion of the etch cycle, the device is removed, and any residual Cr is completely wet-etched, resulting in a monolithic quartz binary grating.

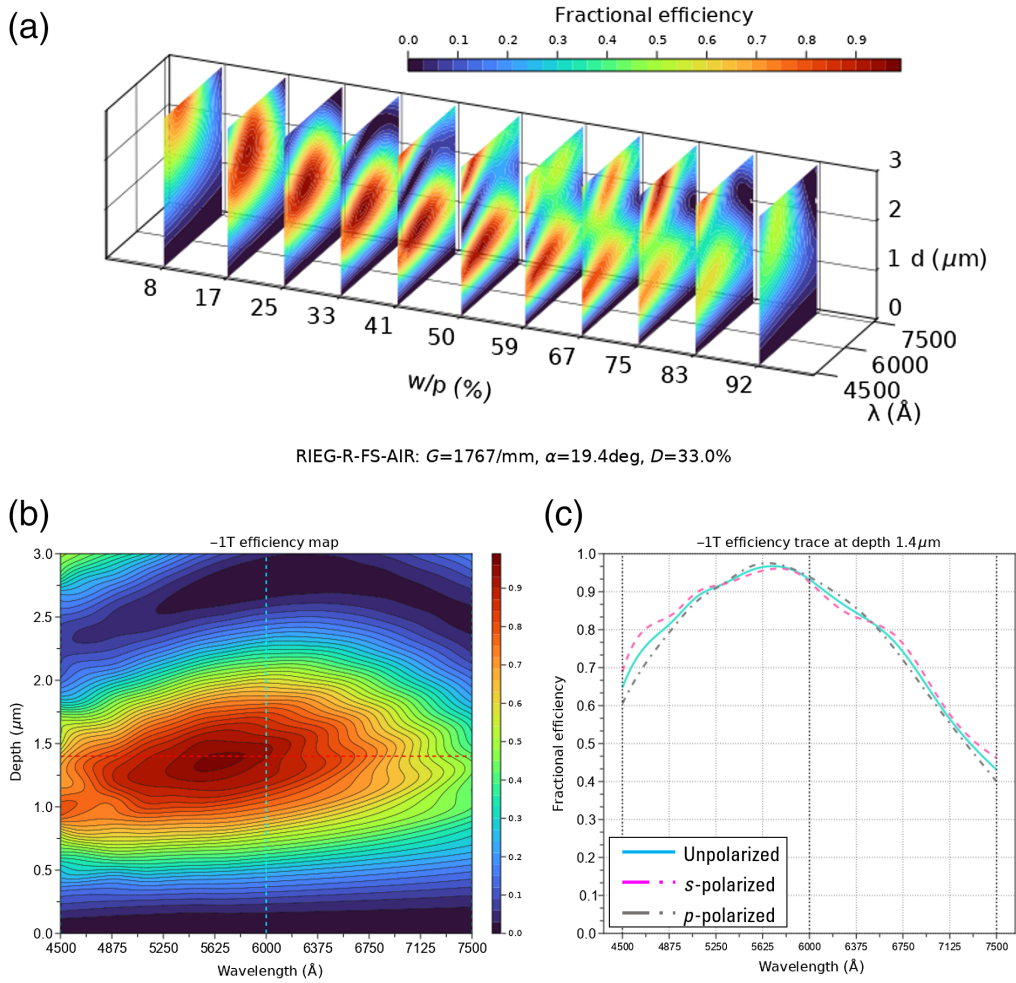


Fig. 2 The first-order DE model of the POC RIPLE grating. (a) Slices of the RCWA computed efficiency cube used in optimizing w and d and (b) the efficiency map over λ and d for $w/p = 33\%$, locating the optimal depth within the range between 1.3 and $1.5 \mu\text{m}$ for maximum overall efficiency. (c) The wavelength slice at $d = 1.4 \mu\text{m}$, where the efficiency peaks at 96.7% and stays over 70% over the wavelength range of 230 nm from 454 to 685 nm . Makie.jl was used to produce these plots.⁶

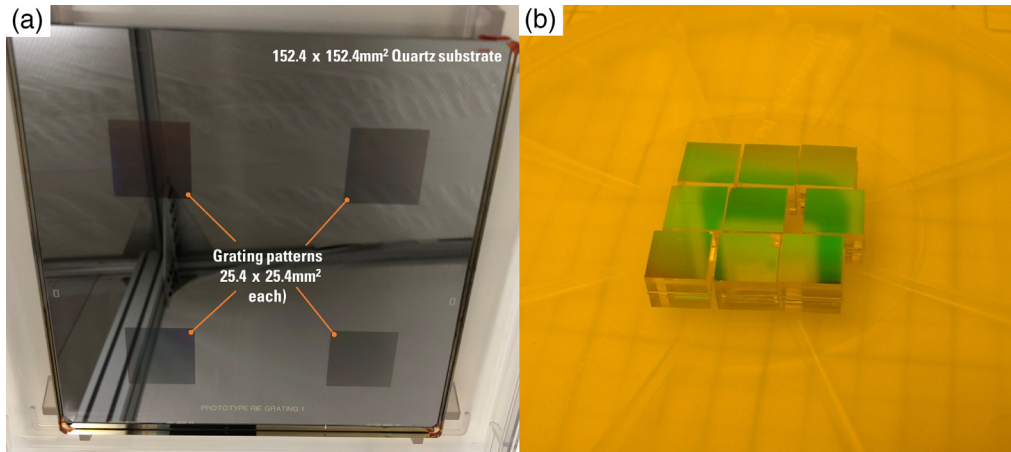


Fig. 3 (a) The electron beam mask for the POC RIPLE grating development. (b) One of the grating quadrants was diced to nine proxies with which the fabrication process was developed.

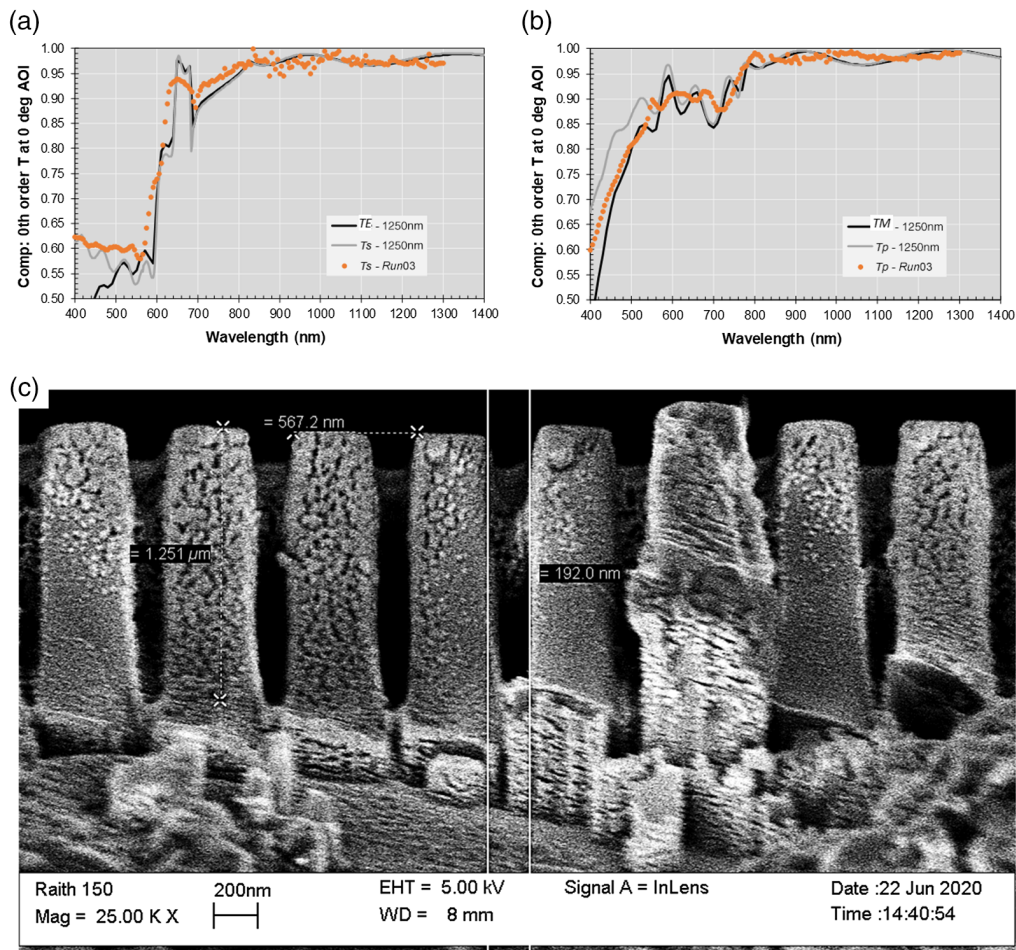


Fig. 4 An example in-process depth verification data of one of the proxies. (a) and (b) The zeroth order s - and p -polarization transmission curves (orange dots) at $\alpha = 0$ deg compared with model predictions given by two RCWA codes, i.e., the GSolver for black solid lines and the UNCCs in-house for gray solid lines. It is worth noting that TE and TM correspond to s - and p -polarization, respectively, in GSolver. The estimated depth from the model comparison was $d = 1250$ nm. (c) The SEM micrograph of a side of the same proxy revealing the proxy grating line morphology. The estimated etch depth, width, and line pitch were 1251, 192, and 567 nm, respectively, with ± 5 nm uncertainty.

The fabrication process parameters were iterated with the proxies to arrive at the design target depth. These proxy gratings were then measured for their zeroth-order transmission using an ellipsometer (Woollam Variable-Angle Spectroscopic Ellipsometer) for both incident polarizations at $\alpha = 0$ deg. The measurements were compared with numerical simulation results to estimate the etch depths achieved in the proxies [Figs. 4(a) and 4(b)]. We used two independent RCWA code bases [one is by GSolver[®] (GSolver[®] is a software tool by Grating Solver Development Company) and one is UNCCs in-house package] to verify the model consistency between fabrication implementations. The two simulations were consistent with each other, particularly for sub-wavelength period scales where critical transmission performance was to be expected (600 to 800 nm). This approach of in-process depth verification through functional testing worked well in estimating the etch depth in comparison with direct imaging of the line structure, as shown in Fig. 4(c). It is worth noting that the visible roughness on the sides of the grating lines resulted from the dicing process of these proxies. We acknowledge, however, that the imaged profile, being a cross-section of a tiny segment, may be regarded as representative only if the assumption of its universality across the entire grating surface is verified. Once the transmission measurement was in agreement with respect to the numerical modeling results for the target depth, the process parameters were used to fabricate a grating on one of the quadrants.

Due to the 9× (and 81×) scale-up in patterned (and substrate) surface area from a proxy to a quadrant-sized device, the net etch rate and plasma saturation conditions had to be re-balanced. We verified that the process does not scale linearly in area, and we performed trials to achieve the desired etch depth on some of the quadrants. This area-scaling process factor will have to be further revised for larger RIPLE gratings that are likely needed for astronomical spectrographs.

3 POC RIPLE Grating Spectral Measurement

The final device was evaluated in transmission for both the zeroth- and first-diffraction order at operational wavelengths and multiple α . For the evaluation, we used the latest evolution of an existing grating tester;⁸ its measurement core is shown in Fig. 5. The core is a simple $4f$ relay system. An unpolarized diverging beam from the fiber bundle output is projected over the first lens (100-mm focal length) with an iris and converted to a properly sized collimated beam. The beam diameter can be adjusted from 2 to 25.4 mm. We set it to 15 mm for all spectral measurements. The grating under test is assembled into its cell. This assembly is then mounted onto the grating mount. The central slot in the grating mount exposes the grating to the incoming collimated beam. The cell contains mechanical features not only to clamp the grating in a fixed position but also to offset the grating both horizontally (via continuous sliding) and vertically (via multiple slots at discrete heights). The offset feature permits the evaluation of the spatial variation of the diffraction performance of larger area gratings used in astronomical spectrographs. Due to the mechanical run-out at the interface surfaces of the grating mount plate, the grating cell, and the grating itself, the actual grating AOI used in any given measurement sequence could only be controlled to ± 0.5 deg with respect to the nominal. The grating mount is on a precision rotary stage. It also sits on the measurement arm where the camera lens (100-mm focal length) and detector (918D-UV-OD3R from Newport) are mounted. This entire arm rotates on another rotary stage. Combinations of the rotary motions of these stages set the grating and the detector to specific angles for spectral measurements. The rotary motions are close-loop controlled to ± 0.05 deg. The center of the grating is mechanically constrained to coincide with the axis of the rotary motions to a machining tolerance of ± 0.25 mm. The light source of the grating tester is a fiber-coupled laser-driven light source (LDLS) from Hamamatsu/Energetiq (EQ-99X-FC-S). The LDLS fiber output is coupled to a monochromator (Cornerstone-130-1/8m) that selects and feeds a test wavelength into the fiber bundle. Each wavelength selection is accurate to ± 0.5 nm with a spectral dispersion of 2.5 nm given by the 760- μm wide slit used. The wavelength selection, rotary motion control, and detector readout are

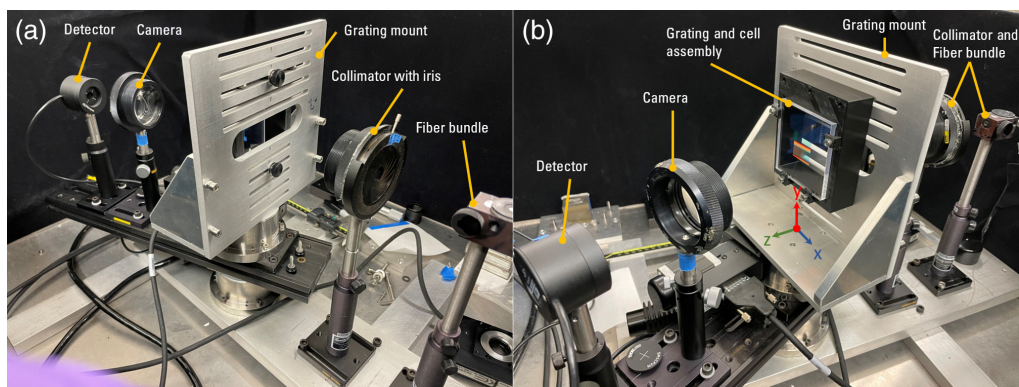


Fig. 5 The grating tester used for final spectral transmission measurements of the POC RIPLE grating. (a) Front view of the tester. Input beam from the fiber bundle is collimated and passes through the horizontal slot in the middle of the grating mount and a grating. Different spatial locations of a grating can be sampled by sliding the grating cell horizontally along five vertically distributed slots. (b) Rear view of the tester with the POC RIPLE grating. The grating mount is on a precision rotary stage. The entire arm from the grating mount to the detector is on another precision rotary stage. Combinations of rotary motions of these stages set the grating and the detector to specific angles for spectral measurements. Both stages rotate about the Y-axis.

all controlled from a software library currently written in Python.⁹ A specific spectral scan is then orchestrated by a user-supplied script layered over the library.

The standard first-order measurement sequence begins with a background measurement (the LDLS input temporarily blocked by a shutter) followed by an initial spectral scan in a straight-through configuration without a grating. This establishes the baseline scan of the tester. The background flux within the tester's chamber is typically <0.1 nW, is stable at this level over time, and is dominated by the detector readout noise (± 0.08 nW). The baseline flux ranges from 1100 nW (near 450 nm) to 300 nW (near 750 nm) due largely to the monochromator transmission profile. Once the grating is inserted and located in the grating mount, the tester is positioned to a set of specific angle combinations for a spectral scan at the first order. The sequence finishes with another spectral scan taken in the same way as the first baseline scan. Because the LDLS flux changes linearly by a few nW over the relatively short (7 min) period of the measurement sequence, two baseline scans are used to linearly interpolate the baseline flux at the time of the first-order scan. This approach typically matches the baseline flux time evolution to $< \pm 1$ nW. This interpolated baseline is used to calibrate out the tester's transmission from the first-order scan, resulting in the grating's first-order transmission. The same sequence is used for the zeroth-order measurement except that the angle combinations are different. Based on these measurement characteristics, we estimate the error in the zeroth- and first-order spectral transmission measurements to be much $< 1\%$.

Figure 6(a) visually shows the dark zeroth and bright dispersed first-order transmission from the finished POC RIPLE grating over a white wall (this was done in a separate set up outside the grating tester; also note that the beam overfills the grating). The light entry side of the grating was anti-reflection treated via nano-textured surface structures as detailed elsewhere.¹⁰ The transmission through this surface was measured (e.g., 99.2% at 450 nm, 99.6% at 625 nm, and 99.4% at 750 nm) and calibrated out from the spectral measurements to yield transmitted DE estimates of the grating. Figure 6(b) shows the unpolarized DE curves in the zeroth (turquoise, $mT0$) and first (orange, $mT1$) order at multiple α . The DE curves in the other diffraction orders (plotted in gray lines) were estimated from the zeroth- and first-order curves. This residual contribution (mTX) is due to the reflective diffraction at the 0th, +1st, -1st, and -2nd orders, as indicated by the POC RIPLE grating model. The first-order DE curve at $\alpha = 19.4$ deg closely resembles the model shown in Fig. 2(c). The model peaks at $DE_p = 96.7\%$ ($\lambda_p = 565$ nm) and stays over 70% from 477 to 707 nm ($\Delta\lambda_{70} = 230$ nm), whereas the measured curve reaches $DE_p = 94.3\%$ ($\lambda_p = 560$ nm) and remains over 70% from 458 to 667 nm ($\Delta\lambda_{70} = 209$ nm). Both DE_p and $\Delta\lambda_{70}$ appear stable across α , i.e., $DE_p = 94\%$ and $\Delta\lambda_{70} = 202$ nm at $\alpha = 18.8$ deg and

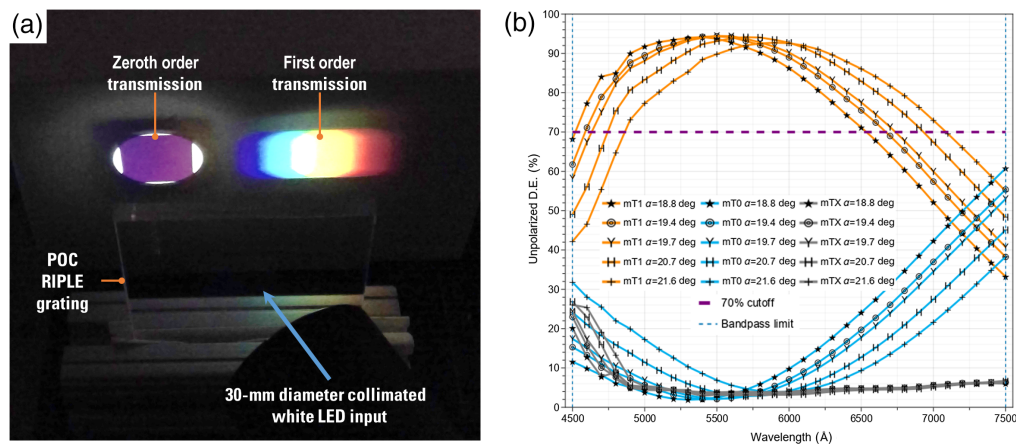


Fig. 6 (a) A visual display of the zeroth- and first-order transmissions through the POC RIPLE grating under a collimated white LED illumination. (b) Spectral scans of the POC RIPLE grating. The measured zeroth-order ($mT0$, turquoise lines) and first-order ($mT1$, orange lines) transmissions at multiple α and 31 wavelength positions. Also plotted (mTX , gray lines) are the transmissions at other diffraction orders estimated by $100 - (mT1 + mT0)$ at each α . Makie.jl was used to produce panel-(b).⁶

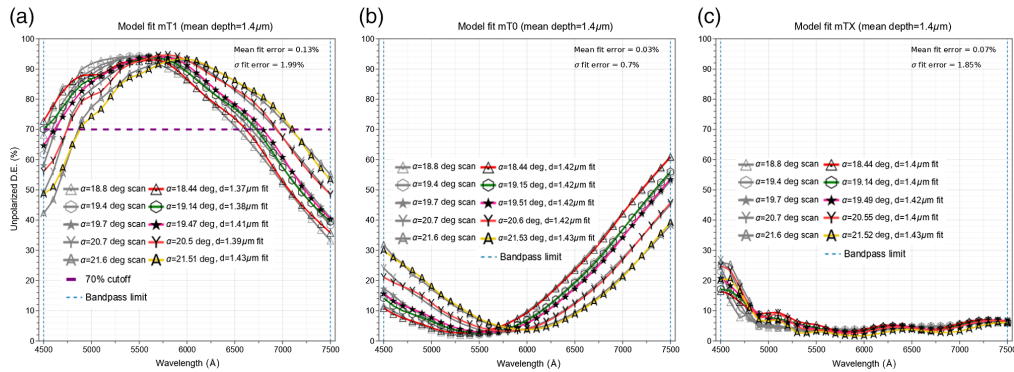


Fig. 7 Measured (or estimated) spectral scans (gray), same as in Fig. 6(b), except overlaid by the model that fits with the best d and α (colored). (a) $mT1$; (b) $mT0$; and (c) mTX . The mean of the best fit depths is $1.4 \mu\text{m}$. The best fit α appears slightly shallower than those used in the measurement but stays well within the ± 0.5 deg uncertainty range estimated in setting up the grating with respect to the grating tester's optical axis. Makie.jl was used to produce these plots.⁶

$DE_p = 92.7\%$ and $\Delta\lambda_{70} = 222 \text{ nm}$ at $\alpha = 21.6$ deg. The zeroth-order DE curves dip down to 2% . This may be translated to 98% $mT1$ peak as frequently done by some grating manufacturers, but the actual $mT1$ scan perhaps warns against such practices due to the possibility of leakage into mTX orders and through other mechanisms (e.g., scattering).

Figure 7 shows the model efficiency curves, as shown in Fig. 2, with optimal d and α that best-fit the measured $mT1$ and $mT0$. The models for the estimated mTX scans were created by averaging the model fits between $mT1$ and $mT0$ for each α . d was constrained within $[1, 3] \mu\text{m}$, and α was limited within ± 0.5 deg with respect to the angles used during the scans. The Levenberg–Marquardt algorithm, as implemented in the Julia programming language¹¹ through the LsqFit.jl package,¹² was used for finding the optimal d and α in the model fit process. The mean depth from the $mT1$ and $mT0$ fits is $1.4 \mu\text{m}$. The $mT1$ models deviate the most from the measurements in wavelengths around 5000 \AA , where the measurements came out slightly higher than the model predictions in Fig. 7(a). This is less obvious in the $mT0$ model fit in Fig. 7(b), but then shows up again in the mTX [Fig. 7(c)]. One interpretation is that the efficiency leakage into mTX orders is somehow less than what the model anticipated. Although the exact cause is yet to be investigated, our preliminary models of grating line defects showed cases in which the angled side walls tended to smooth out sharp variations to slightly higher efficiency at the expense of lowering the peak. It seems too premature to speculate exactly how the final DE is affected by such defects; however, intuitively, any defect would result in the suppression of the DE as observed. An indication from the σ fit error quantity, which represents the rms deviation of the models from the measurements, is that the process developed for fabricating the POC RIPLE grating could be controlled within a few percent of the model prediction, which also implies the presence of a non-significant level of such defects in the device.

4 Conclusion

We detailed the fabrication of a binary phase first-order POC RIPLE grating. The grating featured a near 8:1 high depth-to-width ratio. The electron-beam lithographic patterning process enabled accurate and deterministic creation of the grating surface mask. The in-process spectral scans assisted the reactive ion etching process development to allow us to robustly monitor the etch depth in each etching run. All together, these resulted in a POC RIPLE grating that exhibited near theoretical DE over a broad bandpass as detailed. This type of binary grating can potentially be a high-throughput alternative to Volume-Phase Holographic Gratings (VPHGs) for general spectroscopic applications, in which the RIPLE gratings can serve as main or cross dispersion elements in low, medium, and high-resolution spectrographs not only in ground-based telescopes but also in those subject to challenging conditions such as in space observatories.

For the RIPLE grating to be useful in an astronomical context, two technical aspects warrant further development. The first is a control over the blaze angle of the RIPLE gratings. This arises when a spectrograph needs to operate at an off-Littrow mode. One reason to use a grating in an off-Littrow mode is to avoid the so-called recombination Littrow ghost, the main spectra reflected at lower efficiencies from a detector diffracted and recombined at the grating in reflection and then propagated back to the detector, forming a bright broadband slit image in the middle of the spectra.¹³ As a stay-light precaution, several spectrographs contain gratings specifically designed to push this ghost outside their detector area by physically tilting the gratings while keeping the blaze angle unchanged. The latter is done in VPHGs by adding a few degrees of fringe tilt in the opposite direction to the grating tilt. A similar blaze shift is in principle possible in the RIPLE grating by introducing angular tilts to grating masks during the fabrication process, resulting in physically slanted grating lines.

The second, and perhaps more important aspect that is unique to (ground-based) astronomy is the grating clear aperture diameter of over 100 mm, possibly up to 250 mm. This size range tends to match the beam sizes of many existing and planned spectrographs, although some spectrographs do have a <100 mm diameter.⁵ In comparison with typical devices at the mm-scale dimensions used in photonics and micro-electronics applications, it will be a leap by orders of magnitude and will call for appropriate processes to write and etch (asymmetric) nano-scale grating structures into substrates uniformly over large areas. Our experience suggests that current electron-beam lithography is capable of robustly producing $150 \times 150 \text{ mm}^2$ grating masks with critical feature dimensions down to a few tens of nanometers. Going beyond this in area appears possible for those gratings with feature sizes larger than 400 nm, for which purpose-tuned i-line lithography processes can consistently produce grating masks up to $225 \times 225 \text{ mm}^2$ in size.¹⁴ For much larger feature grating masks, standard laser lithography is available for sizes beyond $250 \times 250 \text{ mm}^2$. Some of the high-end reactive ion etchers with large platen (approaching 0.5 m in diameter), such as PlasmaTherm 7000, should be able to process at least these so-called standard 6- and 9-in. grating masks into large-area RIPLE gratings.

In a broader context, there is a trend of constructing a spectrograph out of multiple smaller identical units, especially in wide-area spectroscopic survey programs under seeing-limited conditions.^{5,15–17} These replicated instruments tend to have beam sizes on a smaller side (150 mm or smaller). This trend could continue for future generations of instruments for the existing telescopes as well as the ELTs. In addition, AO systems will be an important factor to consider, in that AO-assisted spectrographs will be able to achieve the same spectral resolution with a smaller beam size than those of seeing-limited spectrographs. A RIPLE process targeting areas beyond 100×100 up to $150 \times 150 \text{ mm}^2$ could turn out to be most technically feasible and cost-effective method for providing high-efficiency broadband dispersion solutions for future instruments. Our current process development effort, supported by the National Science Foundation, is focused on this area range with additional emphasis on the blaze angle control and gratings with multi-scale line features, all of which we plan to report in the near future.

Acknowledgments

The POC RIPLE grating development was supported by the Cox Endowment Grant from the UT Austin Astronomy Program. The upgrade of the grating tester used in this work was supported by the National Science Foundation as part of the on-going large area RIPLE process development (Grant No. 2107947). We acknowledge fabrication facilities maintenance and support from the Optics Center at the University of North Carolina at Charlotte. The authors thank Toppan Inc. for writing the electron-beam grating mask. The authors have no relevant financial interests in the manuscript and no other potential conflicts of interest to disclose.

References

1. GMT Science Advisory Committee and GMT Project Office, *The Giant Magellan Telescope Science Book 2018*, GMTO Corporation, Pasadena, CA (2018).

2. W. Skidmore, “Thirty meter telescope detailed science case: 2015,” *Res. Astron. Astrophys.* **15**, 1945–2140 (2015).
3. A. H. Bouchez et al., “The Giant Magellan Telescope adaptive optics program,” *Proc. SPIE* **9148**, 300–318 (2014).
4. H. Lee, M. K. Poutous, and C. Brooks, “Surface-relief gratings with anti-reflective nanostructures for panchromatic astronomical low/medium/high resolution spectroscopic surveys,” *Proc. SPIE* **11451**, 739–745 (2020).
5. G. J. Hill et al., “VIRUS2: a next generation replicated integral field spectrograph with wide field and broad wavelength coverage,” *Proc. SPIE* **11447**, 208–221 (2020).
6. S. Danisch and J. Krumbiegel, “Makie.jl: Flexible high-performance data visualization for Julia,” *J. Open Source Softw.* **6**(65), 3349 (2021).
7. B. Wu, A. Kumar, and S. Pamarthy, “High aspect ratio silicon etch: a review,” *J. Appl. Phys.* **108**(5), 051101 (2010).
8. J. J. Adams, G. J. Hill, and P. J. MacQueen, “Volume phase holographic grating performance on the VIRUS-P instrument,” *Proc. SPIE* **7014**, 2423–2432 (2008).
9. G. Van Rossum and F. L. Drake, *Python 3 Reference Manual*, CreateSpace, Scotts Valley, CA (2009).
10. H. Lee, U. Subash, and M. K. Poutous, “Fabrication and evaluation of reactive ion-plasma etched astronomical diffraction grating with anti-reflective surface nanostructures,” *Proc. SPIE* **12188**, 12188–12176 (2022).
11. J. Bezanson et al., “Julia: a fresh approach to numerical computing,” *SIAM Rev.* **59**(1), 65–98 (2017).
12. J. M. White, P. K. Mogensen, and B. Johnson, “LsqFit.jl: basic least-squares fitting in pure Julia,” <https://github.com/JuliaNLSolvers/LsqFit.jl> (2021).
13. E. B. Burgh et al., “Recombination ghosts in Littrow configuration: implications for spectrographs using volume phase holographic gratings,” *Publ. Astron. Soc. Pac.* **119**, 1069–1082 (2007).
14. J. Carroll, personal communication.
15. G. J. Hill et al., “The HETDEX instrumentation: Hobby–Eberly telescope wide-field upgrade and VIRUS,” *Astron. J.* **162**, 298 (2021).
16. R. Bacon et al., “The MUSE second-generation VLT instrument,” *Proc. SPIE* **7735**, 131–139 (2010).
17. A. Aghamousa et al., “The DESI experiment part II: instrument design,” arXiv:1611.00037 (2016).

Hanshin Lee is a research scientist in the McDonald Observatory at the University of Texas at Austin. He received his DPhil degree in astrophysics from the University of Oxford. He led and contributed to the design, construction, and commissioning of the Hobby–Eberly Telescope wide-field upgrade including the Simmons Dark Energy Camera System, HET metrology systems, and facility instruments. His research interests are in multiplexed spectrographs, phase retrieval and wavefront sensing, micro-optical systems, and diffraction gratings for astronomy.

Menelaos K. Poutous received his doctorate degree from the School of Physics at the Georgia Institute of Technology in 1996. He is an associate professor in the Department of Physics and Optical Science at UNC Charlotte. He previously held a principal development engineer’s position at Digital Optics Corporation, and before that, he was a physics lecturer at Emory University. His research interests are in spectroscopy, diffractive micro-optical elements, photolithographic microfabrication, and artificial optical surfaces.